inorganics

MDPI

Article

Structural and Magnetic Properties of Biogenic Nanomaterials Synthesized by *Desulfovibrio* sp. Strain A2

Mikhail S. Platunov [1,*], Yuriy V. Knyazev [2], Olga P. Ikkert [3], Olga V. Karnachuk [3], Anton D. Nikolenko [1], Roman D. Svetogorov [4], Evgeny V. Khramov [4], Mikhail N. Volochaev [2] and Andrey A. Dubrovskiy [2]

[1] Synchrotron Radiation Facility SKIF, Kol'tsovo 630559, Russia
[2] Kirensky Institute of Physics, Federal Research Center KSC SB RAS, Krasnoyarsk 660036, Russia
[3] Department of Plant Physiology, Biotechnology, and Bioinformatics, Tomsk State University, Tomsk 634050, Russia
[4] National Research Center "Kurchatov Institute", Moscow 123182, Russia
[*] Correspondence: m.s.platunov@srf-skif.ru

Abstract: This study explores the phase composition, local atomic structure, and magnetic properties of biogenic nanomaterials synthesized through microbially mediated biomineralization by the sulfate-reducing bacterium *Desulfovibrio* species strain A2 (*Cupidesulfovibrio*). Using X-ray diffraction (XRD), transmission electron microscopy (TEM), Mössbauer spectroscopy, X-ray absorption near-edge structure (XANES) spectroscopy, extended X-ray absorption fine structure (EXAFS) spectroscopy, and magnetic measurements, we identified a mixture of vivianite ($Fe_3(PO_4)_2{\cdot}8H_2O$) and sulfur-containing crystalline phases (α-sulfur). XRD analysis confirmed that the vivianite phase, with a monoclinic I2/m structure, constitutes 44% of the sample, while sulfur-containing phases (α-sulfur, Fddd) account for 56%, likely as a result of bacterial sulfate-reducing activity. X-ray absorption spectroscopy (XAS) and EXAFS revealed the presence of multiple sulfur oxidation states, including elemental sulfur and sulfate (S^{6+}), underscoring the role of sulfur in the sample's structure. Mössbauer spectroscopy identified the presence of ferrihydrite nanoparticles with a blocking temperature of approximately 45 K. Magnetic measurements revealed significant coercivity (~2 kOe) at 4.2 K, attributed to the blocked ferrihydrite nanoparticles. The results provide new insights into the structural and magnetic properties of these microbially mediated biogenic nanomaterials, highlighting their potential applications in magnetic-based technologies.

Keywords: biomineralization; phosphorus recovery; sulfate-reducing bacterium

Academic Editor: Maurizio Peruzzini

Received: 19 November 2024
Revised: 9 January 2025
Accepted: 21 January 2025
Published: 23 January 2025

Citation: Platunov, M.S.; Knyazev, Y.V.; Ikkert, O.P.; Karnachuk, O.V.; Nikolenko, A.D.; Svetogorov, R.D.; Khramov, E.V.; Volochaev, M.N.; Dubrovskiy, A.A. Structural and Magnetic Properties of Biogenic Nanomaterials Synthesized by *Desulfovibrio* sp. Strain A2. *Inorganics* **2025**, *13*, 34. https://doi.org/10.3390/inorganics13020034

1. Introduction

The role of nanomaterials in modern technological development is steadily increasing [1,2]. At the same time, synthesis techniques are evolving rapidly [3,4]. As a result, nanomaterial production methods have become highly diverse, presenting a key challenge: selecting the appropriate synthesis technique for specific applications. One of the simplest and most accessible methods is the so-called top-down approach, where bulk materials are broken down using techniques such as milling, ablation, or explosion [5,6]. Although conceptually straightforward, the top-down approach can be inefficient, costly, and environmentally harmful for certain applications. This is due to its high energy consumption and the need for complex equipment [7,8]. Furthermore, nanomaterials produced through top-down techniques often lack the desired homogeneity and morphology required for many applications.

In contrast, the development of nanomaterials through green chemistry and biogenic methods offers significant potential for improving nanomaterial quality while adopting a more environmentally friendly approach [9,10]. These "green" synthesis methods utilize biological sources such as plants, fungi, flowers, fruits, bacteria, and starch [3,11,12]. The key advantages of these methods include low cost, the absence of toxic chemicals, and an eco-friendly process for producing stable nanostructures.

Recently, there has been a growing trend toward the use of natural products [13], with bio-sourced extracts frequently applied in drug discovery. The green synthesis of nanoparticles using extracts from plants, bacteria, microorganisms, and other biological sources has proven to be more efficient, economical, and environmentally sustainable than conventional chemical methods.

A notable example is *Magnetotactic* bacteria, which organize magnetic nanoparticles within their cells, enabling them to navigate using the planet's geomagnetic field [14]. These bacteria undergo biomineralization, producing magnetite nanoparticles. Interestingly, this biomineralization process can also occur on cell walls during bacterial activity [15]. The structure of these biomineralized products is highly sensitive to external factors that influence cell growth, such as pH levels, cultivation time, and other conditions. It has been demonstrated [16] that biogenic ferrihydrite nanoparticles produced by the *Klebsiella oxytoca* strain undergo transitions through various morphological states during cultivation. These transitions are characterized by the distribution of iron in non-equivalent crystallographic sites. Structural changes are often accompanied by an increase in the average nanoparticle size, as indicated by small-angle X-ray scattering data.

Subtle changes in the local atomic structure and crystallographic distortions of biogenic nanomaterials synthesized via green methods can significantly impact their magnetic properties, including saturation magnetization and even magnetic stiffness. These properties are critical for determining the potential biomedical applications of nanomaterials [17]. Therefore, studying the crystallographic order – and consequently the local electronic properties—of nanomaterials synthesized through green methods is of paramount importance.

In this study, we investigated the phase composition and local crystallographic order in dried sediments produced during the cultivation of *Desulfovibrio* sp. strain A2 (*Cupidesulfovibrio*) bacteria.

2. Results and Discussion

Figure 1 presents the experimental XRD pattern, which shows the intensity plotted against the diffraction angle (2θ), ranging from approximately 5° to 35°. The distinct high-intensity peaks allowed for the identification of two crystalline phases in the sample, as detailed in Table 1. The phase volume fractions were determined to be 44% for the vivianite phase ($Fe_3(PO_4)_2 \cdot 8H_2O$), which has a typical monoclinic structure with space group I2/m, and 56% for sulfur-containing crystal phases (α-sulfur), characterized by an orthorhombic structure with space group Fddd. Additionally, the diffraction pattern contains broad reflections at d-values of 1.4 Å, 1.52 Å, 1.75 Å, 2.53 Å, and 3.32 Å, which may indicate the potential presence of amorphous content or less-ordered phases that cannot be excluded from the sample.

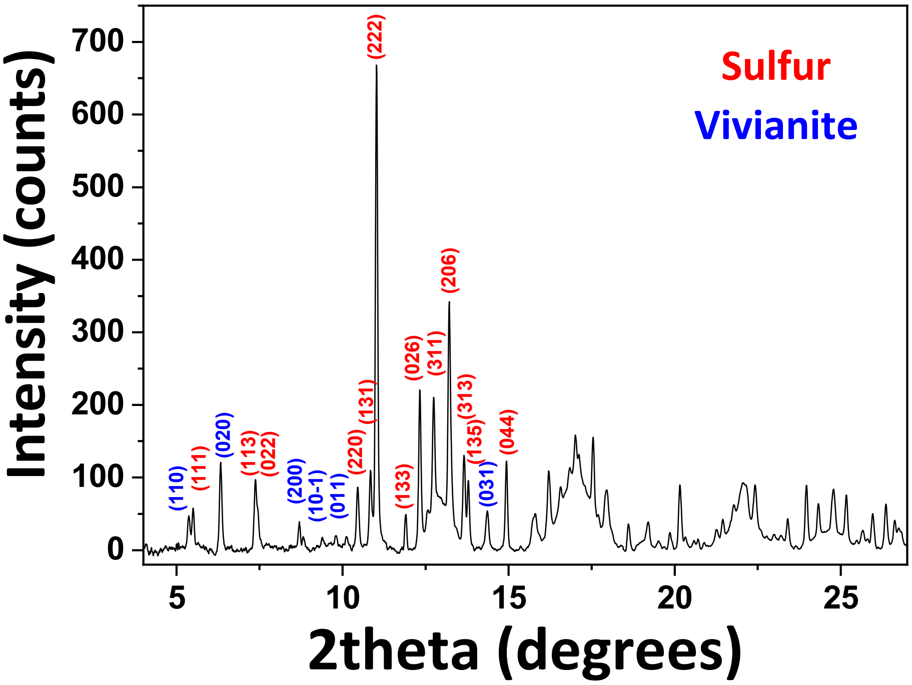

Figure 1. Experimental XRD pattern.

Table 1. Key parameters for the processing and refinement of crystalline phases.

Phase	α-Sulfur	Vivianite ($Fe_3(PO_4)_2 \cdot 8H_2O$)
Space group	Fddd (70)	I2/m (12)
a, Å	10.4674(10)	9.980(16)
b, Å	12.8720(11)	13.413(4)
c, Å	24.4990(22)	4.689(4)
β, deg	90	101.94(3)
Volume, Å^3	3300.9(7)	614.13(30)
Phase volume fraction, %	56.0	44.0
Microstrains, %	0.24	0.50
Scherrer size, nm	>10 µm	>10 µm
Rw, %	1.04	

The sample's morphology was examined using transmission electron microscopy (TEM). Figure 2 shows TEM images of the sample. The analysis reveals that most of the observed area is occupied by nanoparticles, with some crystalline formations also visible. The interplanar distance in the examined local region was determined to be 5.70 Å, which is consistent with the 5.8 Å interplanar spacing characteristic of crystalline sulfur [18]. The observed fringes in Figure 2 correspond to the (022) planes, indicating that sulfur is elongated along the a-axis, with the needle orientation aligned to this axis.

Figure 3 presents the experimental ^{57}Fe Mössbauer spectra recorded over a temperature range of 4.2 to 300 K. At 300 K, the spectrum is characterized by a quadrupole doublet composed of several components: two doublets with parameters similar to those of ferrihydrite and one quadrupole doublet corresponding to the vivianite phase (Table 2). The vivianite phase is identified by the Fe^{2+} state, as indicated by the component with the $\delta = 1.341$ mm/s at room temperature (see Table 2). As shown in previous studies [15], vivianite is a product of microbial life cycle. The relative amount of vivianite remains constant across the entire temperature range, which aligns with our earlier research [15,19]. However, the third ferrihydrite component, usually observed at room temperature, is absent. This absence can be attributed to distortions in the local environment of the iron atoms in the ferrihydrite nanoparticles.

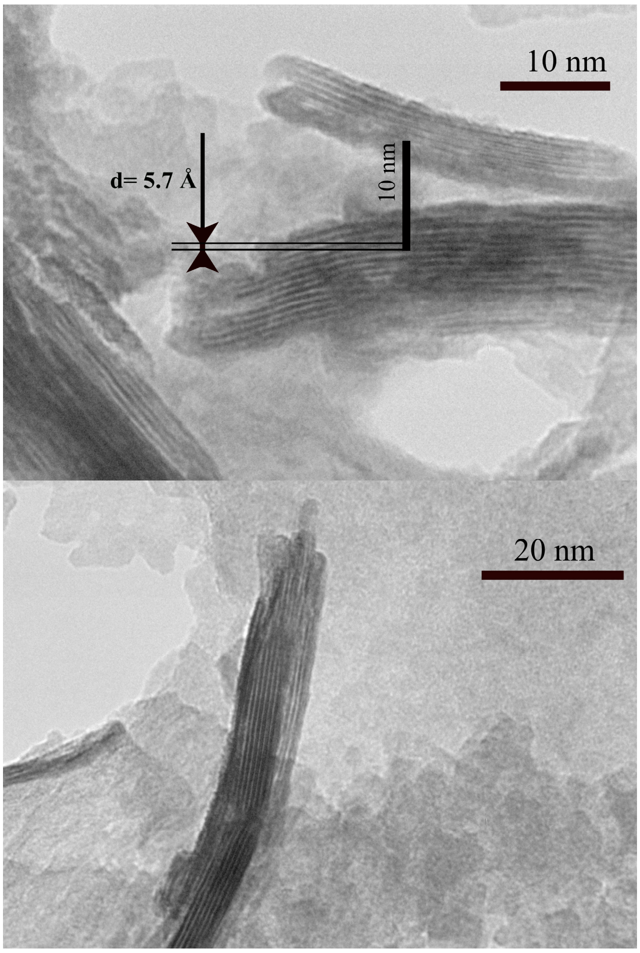

Figure 2. TEM images of the sample captured at different magnifications, illustrating the presence of nanoparticles and crystalline formations.

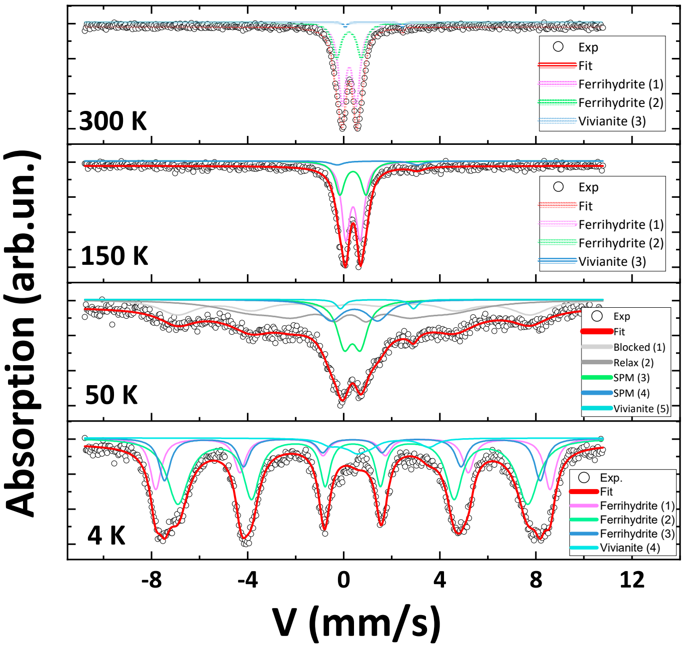

Figure 3. Mössbauer spectra of the sample measured at temperatures ranging from 4 K to 300 K.

Table 2. Mössbauer parameters of the sample at temperatures of 4, 50, 150, and 300 K. The parameter δ represents the chemical shift relative to α-Fe, H_{hf} denotes the hyperfine magnetic field at the iron nuclei, Δ corresponds to the quadrupole splitting, W refers to the full width at half maximum (FWHM) of the Mössbauer peak, dW indicates the line broadening, and A reflects the relative site occupancy.

	δ, mm/s $\pm$0.005	**H_{hf}, kOe $\pm$3**	**Δ, mm/s $\pm$0.01**	**W, mm/s $\pm$0.01**	**dW, mm/s $\pm$0.01**	**A, a.u. $\pm$0.03**	***Origin***
			300 K				
1	0.321	--	0.70	0.458	--	0.78	Ferrihydrite
2	0.506	--	0.71	0.312	--	0.16	
3	1.341	--	2.46	0.093	--	0.06	Vivianite
			150 K				
1	0.449	--	0.60	0.408	--	0.62	Ferrihydrite
2	0.446	--	1.08	0.477	--	0.32	
3	1.458	--	3.33	0.666	--	0.06	Vivianite
			50 K				
1	0.522	456	0	1.814	0.00	0.28	Blocked state
2	0.374	258	0	0.429	2.99	0.40	Relax
3	0.463	--	0.67	0.717	--	0.16	SPM state
4	0.546	--	1.95	1.111	--	0.12	
5	1.487	--	3.04	0.423	--	0.04	Vivianite
			4 K				
1	0.512	510	−0.10	0.567	0.00	0.22	Ferrihydrite
2	0.483	452	0	0.4	0.68	0.54	
3	0.464	486	0.00	0.573	0.00	0.18	
4	1.269	91	3.60	0.879	0.00	0.06	Vivianite

At the low temperature of 4.2 K, the fitting procedure reveals a three-component spectrum, with hyperfine parameters consistent with previous results [15,19]. At intermediate temperatures, the nanoparticles transition from the superparamagnetic (SPM) state to the blocked state via a relaxation process, typical for interacting nanoparticles [20]. Our Mössbauer data do not indicate the presence of iron-sulfur compounds. However, to resolve the possible non-crystalline iron-sulfur bindings, we carried out X-ray absorption spectroscopy (XAS) measurements.

XAS was employed to investigate the electronic properties of sulfur and its interaction with metals. Sulfur is pivotal in sulfate-reducing bacteria, functioning as an electron acceptor, which makes it vital to analyze its electronic configurations within the samples. The sulfur *K*-edge XANES spectrum (Figure 4) reveals that transitions in the near-edge region are primarily governed by dipole-allowed transitions of S 1*s* electrons into unoccupied orbitals with pronounced *p*-character. This provides a sensitive indicator of the sulfur electronic structure.

The sulfur *K*-edge XANES spectra are highly sensitive to sulfur's oxidation state, with absorption edge energies spanning approximately 13 eV between the oxidation states S^{2-} and S^{6+} [21,22]. Different sulfur compounds exhibit distinct absorption-edge features, enabling their differentiation. Leveraging these spectral properties, we used a combined qualitative and quantitative method to determine the relative amounts of sulfur compounds in the sample [21].

As shown in the XANES spectrum (Figure 4a), the presence of sulfur is evident at around 2473 eV, while sulfate (S^{6+}) appears at approximately 2482 eV, and sulfite ($(SO_3)^{2-}$, S^{4+}) lies in between. Using peak fitting techniques, we estimated the relative abundance of the sulfur species to be 3.62 for sulfur, 1.09 for $(SO_3)^{2-}$, and 1.58 for $(SO_4)^{2-}$.

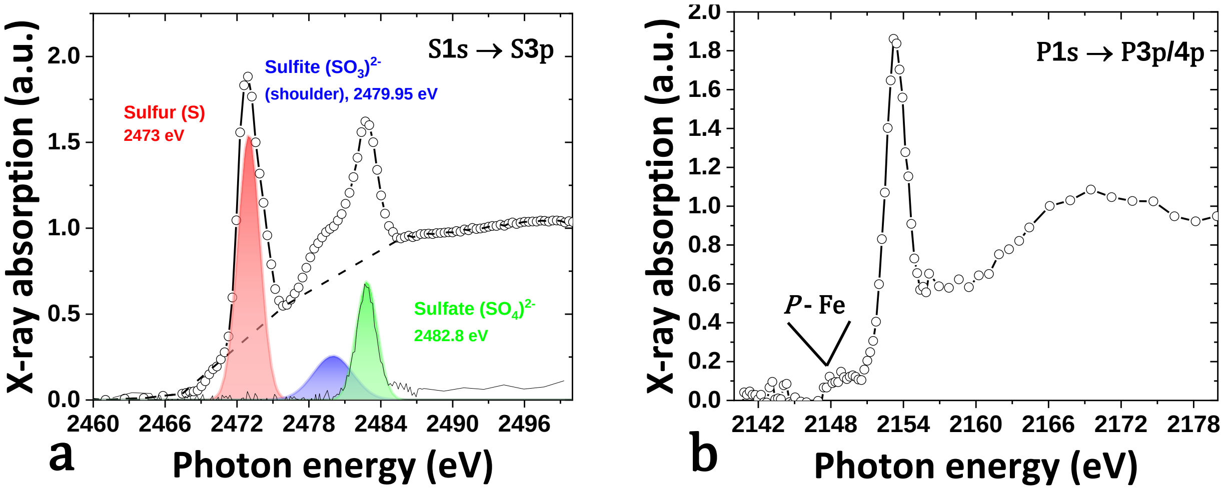

Figure 4. (**a**) Normalized S *K*-edge X-ray absorption spectrum, showing transitions characteristic of sulfur, sulfate $(SO_4)^{2-}$, and sulfite $(SO_3)^{2-}$ oxidation states. For comparison, the experimental sulfur XAS spectrum of a control sample containing only sulfate $(SO_4)^{2-}$ is included. (**b**) Normalized P *K*-edge X-ray absorption near-edge structure (XANES) spectrum of the sample, measured in transmission mode.

The sharp peak at 2482 eV indicates the presence of sulfate species, and the intensity of this peak reflects the relative concentration of sulfates. When various sulfur species coexist, the S *K*-edge XANES spectrum represents a combination of the distinct absorption edges corresponding to each species. This enables the spectrum to approximate a weighted sum of the absorption cross-sections for the different sulfur species, providing an effective method for sulfur speciation.

Phosphorus (P) *K*-edge XAS was also used to investigate the local chemical environment around phosphorous atoms in the sample. This technique is particularly effective for studying phosphorus-containing materials, as it provides detailed insights into covalent metal–phosphorus bonding and redox behavior. The measured P *K*-edge spectrum (Figure 4b) reveals a pre-edge feature at 2150 eV, followed by an intense peak at 2154.2 eV, commonly referred to as the white line, and a broader peak positioned around 2170 eV.

The P *K* pre-edge signal at 2150 eV corresponds to electronic transitions from the P 1*s* orbital to hybridized iron orbitals, indicating the formation of phosphorus–iron bonds [23,24]. This pre-edge feature suggests significant interactions between phosphorus and iron atoms, indicating the formation of phosphate-based structures within the sample. The second peak in the XAS spectrum at a higher energy level corresponds to a dipole-allowed transition, where an electron from the 1*s* orbital is excited into conduction band states associated with P 3*p* and Fe 4*p* orbitals.

Interestingly, this distinctive pre-edge characteristic is typically not observed in the XAS spectra of elemental phosphorus (characterized by P–P bonds) or in metal–phosphorus compounds like CoP and FeP. Similarly, it is absent in phosphate-based solids, including sodium pyrophosphate, KH_2PO_4, or $Co_2(PO_4)_2$ [25–30]. Conversely, this feature is often present in systems where phosphate ions interact with metal (hydr)oxide phases, such as unrefined soil or sediment samples, and in hydrated metal–phosphorus compounds, including materials like vivianite [31–33].

EXAFS analysis offers valuable insights into the local atomic environment around specific elements [34–36]. This non-destructive, element-specific technique is widely applied to study nanostructured materials under standard conditions. Figure 5a shows the normalized Fe *K*-edge XANES spectrum of the sample. The pre-edge feature between 7112 and 7115 eV corresponds to the 1*s*–3*d* transition, with its intensity suggesting that a significant portion of Fe atoms are in octahedral coordination, as indicated by the shape of this feature. The main peak at 7130 eV, linked to the 1*s*–4*p* transition, provides critical information on the electronic structure of the iron atoms.

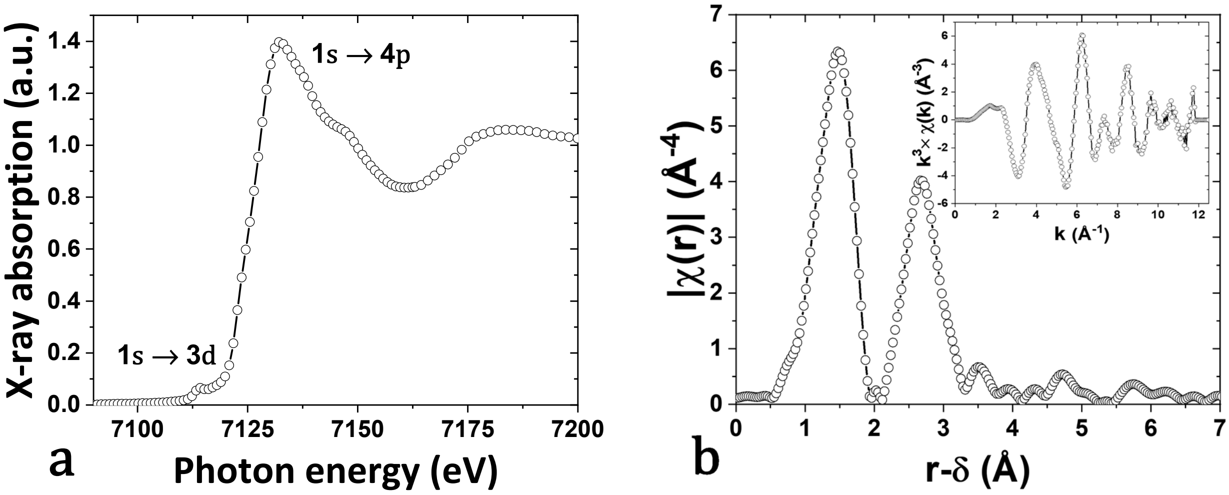

Figure 5. (**a**) Normalized XANES spectrum of the sample measured at the Fe *K*-edge at room temperature. (**b**) Fourier transform (FT) magnitude of the EXAFS spectrum. The k^3-weighted EXAFS experimental function is shown in the inset.

Figure 5b shows the Fourier transform (FT) of the k^3-weighted EXAFS data for the analyzed material. Two primary coordination shells are observed: Fe–O at approximately r-δ = 1.5 Å and Fe–Fe at approximately r-δ = 2.8 Å. Multiple-scattering paths do not significantly influence the EXAFS fitting. During the fitting process, the coordination numbers for the nearest coordination shells (FeO_6) were fixed, while the Debye-Waller factors and interatomic distances were varied. The best fit for the first coordination shell (FeO_6 = 2.02 Å) showed interatomic distances that differ from those of bulk crystalline vivianite. The analysis of the more intricate second coordination shell will be addressed in subsequent research.

Before analyzing the magnetic results, it is important to note that XRD, XANES/EXAFS, and Mössbauer spectroscopy confirm the presence of iron-containing magnetic phases in the sample (vivianite and ferrihydrite nanoparticles). Due to the presence of organic material and crystalline sulfur, only the relative magnetization of the sample can be assessed. Figure 6 shows the temperature dependence of magnetization (M(T)) measured in both ZFC and FC modes under a field strength of 1 kOe. Vivianite is known to exhibit antiferromagnetic behavior, with a Néel temperature (T_N) of approximately 8.8 K [37]. The distinct change in the curvature of the M(T) curve at around 45 K indicates the superparamagnetic blocking of ferrihydrite nanoparticles, consistent with previous studies [15,19].

At 4.2 K, the sample exhibits magnetic hysteresis (Figure 6), with a coercivity (H_C) of around 2 kOe, which aligns with the behavior of blocked ferrihydrite nanoparticles [21]. As the magnetic field increases beyond 50 kOe, the M(H) curve becomes reversible, and the linear behavior observed above 40 kOe suggests possible paramagnetic contributions from both the vivianite and sulfur phases.

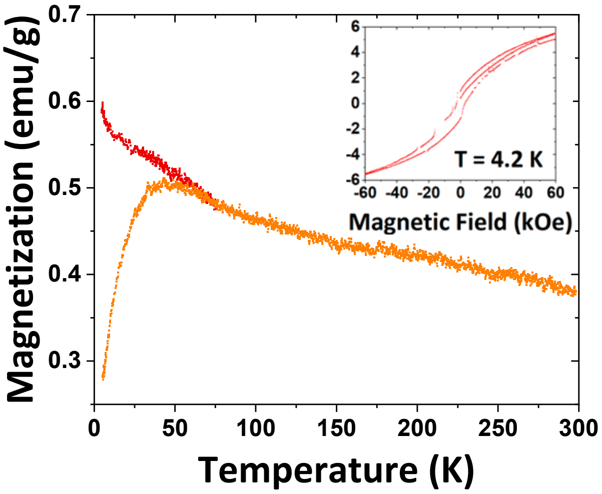

Figure 6. Field-cooled (FC) and zero-field-cooled (ZFC) temperature dependences of magnetization in a magnetic field of 1 kOe. In the inset: field dependence of the sample's magnetization at 4.2 K.

3. Experimental Details

3.1. Microbial Cultures and Mineral Formation Processes

The studied sample was derived using a sulfate-reducing bacterium (SRB), specifically *Desulfovibrio* sp. strain A2, under anaerobic conditions. This strain has been thoroughly investigated in [38]. The biological culture was cultivated anaerobically in standard Widdel–Bak medium [39], which contains the following salts at the specified concentrations per liter: Na_2SO_4 (4.0 g), KH_2PO_4 (0.2 g), NH_4Cl (0.25 g), NaCl (1 g), $MgCl_2 \cdot 6H_2O$ (0.4 g), KCl (0.5 g), and $CaCl_2$ (0.113 g). Additionally, pure metallic iron was included in the cultivation process, as detailed in [40]. The medium contained 0.423 mg/L of soluble iron, with 18 mM lactate serving as the electron donor. The culture was grown in 500 mL serum bottles at 28 °C for six days. Following incubation, precipitates were collected via centrifugation at $5000\times\ g$ for 10 min, air-dried, and manually ground.

3.2. Measurement Methods

Initially, X-ray diffraction measurements were performed on a Bruker D8 ADVANCE laboratory diffractometer, utilizing Cu-$K\alpha$ radiation and a VANTEC linear detector for data acquisition (Krasnoyarsk, Russia). However, the signal obtained from this laboratory setup was insufficient for high-quality analysis. To address this, additional X-ray diffraction measurements were performed at a synchrotron station, where the significantly higher brightness of synchrotron radiation and the use of a 2D detector enabled superior diffraction patterns. The X-ray powder diffraction (XRD) experiments were performed at room temperature at the Belok/RSA beamline at the "KISI-Kurchatov" synchrotron facility in Moscow, Russia [41]. Monochromatic radiation with a wavelength of $\lambda = 0.74$ Å was focused onto the sample with a beam size of $400 \times 400\ \mu m^2$. The experiments were performed in Debye–Scherrer geometry (transmission mode), with the sample placed in a 200 µm cryo-loop using immersion oil. During the measurements, the sample was rotated around a horizontal axis to average the diffraction patterns across various sample orientations, thereby enhancing the accuracy and reliability of the collected data.

The diffraction patterns were captured using a two-dimensional Rayonix SX165 detector, placed 150 mm away from the sample at a 29.5° angle relative to the synchrotron beam. The resulting 2D diffraction data were integrated into one-dimensional intensity profiles, I(2θ), utilizing the Dionis software [42]. To ensure accuracy, the detector's angular alignment was calibrated, and the diffraction peak broadening caused by the instrument was assessed using the LaB_6 polycrystalline sample (NIST SRM 660a). The structural parameters of the samples, as well as phase ratios, were subsequently determined through full-profile analysis of the diffraction data using the Rietveld refinement method within the GSAS II software [43].

Transmission electron micrographs and SAED (selected area electron diffraction) patterns were obtained using a Hitachi HT7700 microscope (Krasnoyarsk, Russia). An accelerating voltage of 100 kV was applied to the electron beam. Specimens were prepared by dispersing nanoparticle powder in alcohol using an ultrasonic bath and depositing the suspension onto support grids with a perforated carbon coating.

Fe *K*-edge extended X-ray absorption fine structure (EXAFS) measurements were performed at the Structural Materials Science beamline of the Kurchatov Synchrotron Radiation Source in Moscow, Russia [44]. The data were obtained at ambient temperature in transmission mode, employing a channel-cut Si(111) monochromator to achieve an energy resolution of approximately $\Delta E/E \sim 2 \times 10^{-4}$. Ionization chambers filled with carefully selected N_2–Ar gas mixtures were used for detection. The X-ray beam had a spot size of about 0.5 mm × 0.5 mm, and the energy range covered 200 eV below to 800 eV above the Fe *K*-absorption edge.

EXAFS data were processed utilizing the VIPER [45,46] and IFEFFIT 1.2.11 [47] software tools. The raw spectra were normalized, and background signals attributed to atomic effects were removed. Radial distribution functions around Fe atoms were determined through the Fourier transformation of the k^3-weighted EXAFS signals, analyzed over a wave number range from 2.00 to 11.75 $Å^{-1}$. Structural characteristics such as bond lengths, coordination numbers, and Debye–Waller factors were extracted through non-linear optimization of theoretical models applied to experimental data. The FEFF software was employed to simulate both single- and multiple-scattering effects [48].

X-ray absorption measurements were also performed at the Cosmos beamline of the VEPP-4M storage ring at the Budker Institute of Nuclear Physics (SB RAS) in Novosibirsk [49]. The storage ring operated at an energy of 2.5 GeV with a beam current averaging 7 mA. The synchrotron radiation was monochromatized using a double-crystal monochromator equipped with Si(111) crystals. Measurements of sulfur and phosphorus *K*-edge spectra were obtained in total fluorescence yield mode, utilizing a high-precision silicon photodiode detector (SPD) [50]. Samples were prepared by embedding the powdered sample into a 1 cm × 1 cm × ~50 μm piece of polymethyl methacrylate (PMMA [51]). All measurements were performed at room temperature.

The ^{57}Fe Mössbauer spectroscopy measurements were performed with an MS-1104Em spectrometer from the Research Institute of Physics, Southern Federal University, operating in transmission geometry. A ^{57}Co radiation source in a Rh matrix was used for nuclear radiation. For experiments within the temperature range of 4 to 300 K, a CFSG-311-MESS cryostat, utilizing a closed-cycle Gifford-McMahon cooling system (manufactured by Cryotrade Engineering, LLC), was used. The spectral analysis involved fitting the experimental data through a least-squares method in a linear framework, with all hyperfine parameters systematically optimized during the fitting process.

The magnetization curves in zero-field cooling (ZFC) and field cooling (FC) modes were obtained using a vibrating sample magnetometer (VSM) with the Quantum Design PPMS-6000 system, as well as a hand-made VSM [52].

4. Conclusions

This study presents a comprehensive analysis of biogenic nanomaterials synthesized by *Desulfovibrio* sp. strain A2 (*Cupidesulfovibrio*), focusing on their phase composition, local atomic structure, and magnetic properties. Using a combination of XRD, TEM, Mössbauer spectroscopy, XANES, EXAFS, and magnetic measurements, we have gained a detailed understanding of these bio-synthesized materials, which consist of a mixture of crystalline sulfur-containing phases, vivianite ($Fe_3(PO_4)_2 \cdot 8H_2O$), and ferrihydrite nanoparticles.

Vivianite, a mineral typically formed in reducing environments, was identified through XRD, with reflections corresponding to the monoclinic I2/m space group. Synchrotron XRD also revealed the presence of sulfur-containing crystalline phases (α-sulfur, Fddd sp.gr.), which account for approximately 56% of the sample. This significant sulfur content likely results from the sulfate-reducing activity of *Desulfovibrio* sp. strain A2 (*Cupidesulfovibrio*), facilitating the incorporation of sulfur into the precipitates.

XAS and EXAFS analyses confirmed the critical role of sulfur in the structural composition of the nanomaterials. The sulfur *K*-edge XANES spectrum revealed peaks associated with sulfur and sulfate (S^{6+}), indicating the presence of multiple sulfur oxidation states, consistent with the metabolic processes of sulfate-reducing bacteria.

Magnetic measurements demonstrated hard magnetic behavior at 4.2 K, suggesting that the biogenic synthesis process produces materials with potentially unique magnetic properties.

The findings of the present paper highlight the potential of sulfate-reducing bacteria in synthesizing biogenic nanomaterials with adjustable phase composition and magnetic properties. Future research should focus on controlling phase formation, evaluating functional applications (e.g., catalysis, energy storage, magnetic devices), and assessing scalability for industrial use.

Author Contributions: M.S.P.: Writing—review and editing, Writing—original draft, Visualization, Supervision, Project administration, Methodology, Investigation, Funding acquisition, Data curation, Conceptualization. Y.V.K.: Conceptualization, Investigation, Data curation, Visualization, Writing—Original draft, Methodology, Software, Writing—review and editing. O.P.I.: Investigation. O.V.K.: Investigation. A.D.N.: Investigation. R.D.S.: Investigation. E.V.K.: Investigation. M.N.V.: Investigation. A.A.D.: Investigation. All authors have read and agreed to the published version of the manuscript.

Funding: This work was supported by the Ministry of Science and Higher Education of the Russian Federation (Agreement No. 075-15-2022-263).

Data Availability Statement: The datasets generated and analyzed during this study, including the raw spectra, are available from the corresponding author upon reasonable request.

Acknowledgments: The investigations were performed using the large-scale research facility 'EXAFS Spectroscopy Beamline' at the Siberian Synchrotron and Terahertz Radiation Center in Novosibirsk, Russia. The electron microscopy and Mössbauer spectroscopy studies were carried out on the equipment of the Krasnoyarsk Territorial Center for Collective Use, Krasnoyarsk Scientific Center, Siberian Branch of the Russian Academy of Sciences.

Conflicts of Interest: The authors declare that they have no known competing financial interests or personal relationships that could have appeared to influence the work reported in this paper.

References

1. Wadhawan, S.; Jain, A.; Nayyar, J.; Mehta, S.K. Role of nanomaterials as adsorbents in heavy metal ion removal from wastewater: A review. *J. Water Process Eng.* **2020**, *33*, 101038. [CrossRef]
2. Pandey, P. Role of nanotechnology in electronics: A review of recent developments and patents. *Recent Pat. Nanotechnol.* **2022**, *16*, 45–66. [CrossRef]
3. Pandit, C.; Roy, A.; Ghotekar, S.; Khusro, A.; Islam, M.N.; Emran, T.B.; Lam, S.E.; Khandaker, M.U.; Bradley, D.A. Biological agents for synthesis of nanoparticles and their applications against plant pathogens. *J. King Saud Univ.-Sci.* **2024**, *34*, 101869. [CrossRef]
4. Huston, M.; DeBella, M.; DiBella, M.; Gupta, A. Green synthesis of nanomaterials. *Nanomaterials* **2021**, *11*, 2130. [CrossRef] [PubMed]
5. Baig, N.; Kammakakam, I.; Falath, W. Nanomaterials: A review of synthesis methods, properties, recent progress, and challenges. *Mater. Adv.* **2021**, *2*, 1821–1871. [CrossRef]

6. Abid, N.; Khan, A.M.; Shujait, S.; Chaudhary, K.; Ikram, M.; Imran, M.; Haider, J.; Khan, M.; Khan, Q.; Maqbool, M. Synthesis of nanomaterials using various top-down and bottom-up approaches, influencing factors, advantages, and disadvantages: A review. *Adv. Colloid Interface Sci.* **2022**, *300*, 102597. [CrossRef]
7. Jiang, Z.; Li, L.; Huang, H.; He, W.; Ming, W. Progress in laser ablation and biological synthesis processes: "Top-Down" and "Bottom-Up" approaches for the green synthesis of Au/Ag nanoparticles. *Int. J. Mol. Sci.* **2022**, *23*, 14658. [CrossRef]
8. Vijayaram, S.; Razafindralambo, H.; Sun, Y.-Z.; Vasantharaj, S.; Ghafarifarsani, H.; Hoseinifar, S.H.; Raeeszadeh, M. Applications of green synthesized metal nanoparticles—A review. *Biol. Trace Elem. Res.* **2024**, *202*, 360–386. [CrossRef]
9. Diallo, A.; Manikandan, E.; Rajendran, V.; Maaza, M. Physical & enhanced photocatalytic properties of green synthesized SnO_2 nanoparticles via Aspalathus linearis. *J. Alloys Compd.* **2016**, *681*, 561–570. [CrossRef]
10. Dwivedi, A.D.; Gopal, K. Biosynthesis of silver and gold nanoparticles using Chenopodium album leaf extract. *Colloids Surf. A Physicochem. Eng. Asp.* **2010**, *369*, 27–33. [CrossRef]
11. Ghidan, A.Y.; Al-Antary, T.M.; Awwad, A.M. Green synthesis of copper oxide nanoparticles using Punica granatum peels extract: Effect on green peach aphid. *Environ. Nanotechnol. Monit. Manag.* **2016**, *6*, 95–98. [CrossRef]
12. Geetha, M.S.; Nagabhushana, H.; Shivananjaiah, H.N. Green mediated synthesis and characterization of ZnO nanoparticles using Euphorbia Jatropa latex as reducing agent. *J. Sci. Adv. Mater. Devices* **2016**, *1*, 301–310. [CrossRef]
13. Hussain, I.; Singh, N.B.; Singh, A.; Singh, H.; Singh, S.C. Green synthesis of nanoparticles and its potential application. *Biotechnol. Lett.* **2016**, *38*, 545–560. [CrossRef]
14. Faivre, D.; Schuler, D. Magnetotactic bacteria and magnetosomes. *Chem. Rev.* **2008**, *108*, 4875–4898. [CrossRef]
15. Knyazev, Y.V.; Platunov, M.S.; Ikkert, O.P.; Semenov, S.V.; Bayukov, O.A.; Nikolenko, A.D.; Nazmov, V.P.; Volochaev, M.N.; Dubrovskiy, A.A.; Molokeev, M.S.; et al. Microbially mediated synthesis of vivianite by Desulfosporosinus on the way to phosphorus recovery. *Environ. Sci. Adv.* **2024**, *3*, 897–911. [CrossRef]
16. Stolyar, S.V.; Bayukov, O.A.; Balaev, D.A.; Ladygina, V.P.; Yaroslavtsev, R.N.; Knyazev, Y.V.; Balasoiu, M.; Kolenchukova, O.A.; Iskhakov, R.S. Ferrihydrite nanoparticles produced by Klebsiella oxytoca: Structure and properties dependence on the cultivation time. *Adv. Powder Technol.* **2022**, *33*, 103692. [CrossRef]
17. Oksel, C.; Ma, C.Y.; Liu, J.J.; Wilkins, T.; Wang, X.Z. (Q)SAR modelling of nanomaterial toxicity: A critical review. *Particuology* **2015**, *21*, 1–19. [CrossRef]
18. Mirkin, L.I. *Powder X-Ray Analysis: Handbook of X-Ray Analysis of Polycrystalline Material*; Translated from the Russian Edition (Moscow, 1961) by J. E. S. Bradley; Consultants Bureau: New York, NY, USA, 1964; p. 731.
19. Knyazev, Y.V.; Ikkert, O.P.; Semenov, S.V.; Volochaev, M.N.; Molokeev, M.S.; Platunov, M.S.; Khramov, E.V.; Dubrovskiy, A.A.; Shestakov, N.P.; Smorodina, E.D.; et al. Superparamagnetic blocking and magnetic interactions in nanoferrihydrite adsorbed on biomineralized nanorod-shaped Fe_3S_4 crystallites. *J. Alloys Compd.* **2022**, *923*, 166346. [CrossRef]
20. Mørup, S.; Madsen, D.E.; Frandsen, C.; Bahl, C.R.H.; Hansen, M.F. Experimental and theoretical studies of nanoparticles of antiferromagnetic materials. *J. Phys. Condens. Matter* **2007**, *19*, 213202. [CrossRef]
21. Almkvist, G.; Boye, K.; Persson, I. K-edge XANES analysis of sulfur compounds: An investigation of the relative intensities using internal calibration. *J. Synchrotron Radiat.* **2010**, *17*, 683–688. [CrossRef]
22. Pin, S.; Huthwelker, T.; Brown, M.A.; Vogel, F. Combined sulfur *K*-edge XANES–EXAFS study of the effect of protonation on the sulfate tetrahedron in solids and solutions. *J. Phys. Chem. A* **2013**, *117*, 8368–8376. [CrossRef] [PubMed]
23. Prietzel, J.; Klysubun, W. Phosphorus *K*-edge XANES spectroscopy has probably often underestimated iron oxyhydroxide-bound P in soils. *J. Synchrotron Radiat.* **2018**, *25*, 1736–1744. [CrossRef] [PubMed]
24. Franke, R.; Hormes, J. The P *K*-near edge absorption spectra of phosphates. *Phys. B Condens. Matter* **1995**, *216*, 85–95. [CrossRef]
25. Yoshida, M.; Mineo, T.; Mitsutomi, Y.; Yamamoto, F.; Kurosu, H.; Takakusagi, S.; Asakura, K.; Kondoh, H. Structural relationship between CoO_6 cluster and phosphate species in a cobalt-phosphate water oxidation catalyst investigated by Co and P *K*-edge XAFS. *Chem. Lett.* **2016**, *45*, 277–279. [CrossRef]
26. Franke, R. X-ray absorption and photoelectron spectroscopy investigation of binary nickelphosphides. *Spectrochim. Acta Part A Mol. Biomol. Spectrosc.* **1997**, *53*, 933–941. [CrossRef]
27. Yin, Z.; Kasrai, M.; Bancroft, G.M.; Tan, K.H.; Feng, X. X-ray-absorption spectroscopic studies of sodium polyphosphate glasses. *Phys. Rev. B* **1995**, *51*, 742. [CrossRef]
28. Prietzel, J.; Dümig, A.; Wu, Y.; Zhou, J.; Klysubun, W. Synchrotron-based P *K*-edge XANES spectroscopy reveals rapid changes of phosphorus speciation in the topsoil of two glacier foreland chronosequences. *Geochim. Cosmochim. Acta* **2013**, *108*, 154–171. [CrossRef]
29. Werner, F.; Prietzel, J. Standard protocol and quality assessment of soil phosphorus speciation by P *K*-edge XANES spectroscopy. *Environ. Sci. Technol.* **2015**, *49*, 10521–10528. [CrossRef]
30. Vogel, C.; Rivard, C.; Wilken, V.; Muskolus, A.; Adam, C. Performance of secondary P-fertilizers in pot experiments analyzed by phosphorus X-ray absorption near-edge structure (XANES) spectroscopy. *Ambio* **2018**, *47*, 62–72. [CrossRef]

31. Beauchemin, S.; Hesterberg, D.; Chou, J.; Beauchemin, M.; Simard, R.R.; Sayers, D.E. Speciation of phosphorus in phosphorus-enriched agricultural soils using X-ray absorption near-edge structure spectroscopy and chemical fractionation. *J. Environ. Qual.* **2003**, *32*, 1809–1819. [CrossRef]
32. Rouff, A.A.; Rabe, S.; Nachtegaal, M.; Vogel, F. X-ray absorption fine structure study of the effect of protonation on disorder and multiple scattering in phosphate solutions and solids. *J. Phys. Chem. A* **2009**, *113*, 6895–6903. [CrossRef] [PubMed]
33. Donahue, C.M.; Daly, S.R. Ligand K-edge XAS studies of metal-phosphorus bonds: Applications, limitations, and opportunities. *Comments Inorg. Chem.* **2018**, *38*, 54–78. [CrossRef]
34. Kuzmin, A.; Chaboy, J. EXAFS and XANES analysis of oxides at the nanoscale. *IUCrJ* **2014**, *1*, 571–589. [CrossRef]
35. Rehr, J.J.; Albers, R.C. Theoretical approaches to X-ray absorption fine structure. *Rev. Mod. Phys.* **2000**, *72*, 621. [CrossRef]
36. Lee, P.A.; Citrin, P.H.; Eisenberger, P.T.; Kincaid, B.M. Extended X-ray absorption fine structure—Its strengths and limitations as a structural tool. *Rev. Mod. Phys.* **1981**, *53*, 769. [CrossRef]
37. Frederichs, T.; von Dobeneck, T.; Bleil, U.; Dekkers, M.J. Towards the identification of siderite, rhodochrosite, and vivianite in sediments by their low-temperature magnetic properties. *Phys. Chem. Earth Parts A/B/C* **2003**, *28*, 669–679. [CrossRef]
38. Karnachuk, O.V.; Sasaki, K.; Gerasimchuk, A.L.; Sukhanova, O.; Ivasenko, D.A.; Kaksonen, A.H.; Puhakka, J.A.; Tuovinen, O.H. Precipitation of Cu-sulfides by copper-tolerant Desulfovibrio isolates. *Geomicrobiol. J.* **2008**, *25*, 219–227. [CrossRef]
39. Widdel, F.; Bak, F. Gram-negative mesophilic sulfate-reducing bacteria. In *The Prokaryotes: A Handbook on the Biology of Bacteria: Ecophysiology, Isolation, Identification, Applications*; Springer: New York, NY, USA, 1992; pp. 3352–3378. [CrossRef]
40. Karnachuk, O.V.; Pimenov, N.V.; Yusupov, S.K.; Frank, Y.A.; Puhakka, Y.A.; Ivanov, M.V. Distribution, diversity, and activity of sulfate-reducing bacteria in the water column in Gek-Gel Lake, Azerbaijan. *Microbiology* **2006**, *75*, 82–89. [CrossRef]
41. Svetogorov, R.D.; Dorovatovskii, P.V.; Lazarenko, V.A. Belok/XSA diffraction beamline for studying crystalline samples at Kurchatov Synchrotron Radiation Source. *Cryst. Res. Technol.* **2020**, *55*, 1900184. [CrossRef]
42. Svetogorov, R.D. *Dionis—Diffraction Open Integration Software*; State Registration Certificate of Computer Program No. 2018660965; LC Scientific Electronic Library: Moscow, Russia, 2018.
43. Toby, B.H.; Von Dreele, R.B. GSAS-II: The genesis of a modern open-source all purpose crystallography software package. *J. Appl. Crystallogr.* **2013**, *46*, 544–549. [CrossRef]
44. Chernyshov, A.A.; Veligzhanin, A.A.; Zubavichus, Y.V. Structural Materials Science end-station at the Kurchatov Synchrotron Radiation Source: Recent instrumentation upgrades and experimental results. *Nucl. Instrum. Methods Phys. Res. Sect. A Accel. Spectrometers Detect. Assoc. Equip.* **2009**, *603*, 95–98. [CrossRef]
45. Klementev, K.V. Package "VIPER (visual processing in EXAFS researches) for windows". *Nucl. Instrum. Methods Phys. Res. Sect. A: Accel. Spectrometers Detect. Assoc. Equip.* **2000**, *448*, 299–301. [CrossRef]
46. Klementev, K.V. Extraction of the fine structure from X-ray absorption spectra. *J. Phys. D Appl. Phys.* **2001**, *34*, 209. [CrossRef]
47. Newville, M. IFEFFIT: Interactive XAFS analysis and FEFF fitting. *J. Synchrotron Radiat.* **2001**, *8*, 322–324. [CrossRef]
48. Zabinsky, S.I.; Rehr, J.J.; Ankudinov, A.; Albers, R.C.; Eller, M.J. Multiple-scattering calculations of X-ray absorption spectra. *Phys. Rev. B* **1995**, *52*, 2995. [CrossRef]
49. Zavertkin, P.S.; Ivlyushkin, D.V.; Mashkovtsev, M.R.; Nikolenko, A.D.; Sutormina, S.A.; Chkhalo, N.I. Vacuum Ultraviolet and Soft X-ray Broadband Monochromator for a Synchrotron Radiation Metrological Station. *Optoelectron. Instrum. Data Process.* **2019**, *55*, 107–114. [CrossRef]
50. Zabrodsky, V.V.; Aruev, P.N.; Sukhanov, V.L.; Zabrodskaya, N.V.; Ber, B.J.; Kasantsev, D.Y.; Alekseyev, A.G. Silicon Precision Detectors for Near IR, Visible, UV, XUV and Soft X-ray Spectral Range. In Proceedings of the 9th International Symposium on Measurement Technology and Intelligent Instruments, Saint-Petersburg, Russia, 29 June–2 July 2009; pp. 243–247.
51. Nazmov, V.P.; Varand, A.V.; Mikhailenko, M.A.; Goldenberg, B.G.; Prosanov, I.Y.; Gerasimov, K.B. Polymethyl Methacrylate with a Molecular Weight of 107 g/mol for X-ray Lithography. *J. Surf. Investig. X-Ray Synchrotron Neutron Tech.* **2023**, *17*, 652–655. [CrossRef]
52. Balaev, A.D.; Boyarshinov, Y.V.; Karpenko, M.M.; Khrustalev, B.P. Automated magnetometer with superconducting solenoid. *Prib. Tekh. Eksp.* **1985**, *3*, 167.